Kobe University Repository : Kernel

PDF issue: 2026-11-26

Topotactic Epitaxy of SrTiO3 Mesocrystal Superstructures with Anisotropic Construction for Efficient Overall Water Splitting

Zhang, Peng ; Ochi, Tomoya ; Fujitsuka, Mamoru ; Kobori, Yasuhiro ; Majima, Tetsuro ; Tachikawa, Takashi

(Citation)
Angewandte Chemie International Edition,56(19):5299-5303

(Issue Date)
2017-05-02

(Resource Type)
journal article

(Version)
Accepted Manuscript

(Rights)
© 2017 Wiley-VCH Verlag GmbH & Co. KGaA, Weinheim. This is the peer reviewed version of the following article: [Angewandte Chemie-International Edition, 56(19):5299-5303, 2017], which has been published in final form at http://dx.doi.org/10.1002/anie.201702223. This article may be used for non-commercia…

(URL)
https://hdl.handle.net/20.500.14094/90004654

Topotactic Epitaxy of $SrTiO_3$ Mesocrystal Superstructures with Anisotropic Construction for Efficient Overall Water Splitting

Peng Zhang,[a] Tomoya Ochi,[b] Mamoru Fujitsuka,[a] Yasuhiro Kobori,[b,c] Tetsuro Majima,*[a] and Takashi Tachikawa*[b,c,d]

Abstract: The higher-order structures of semiconductor-based photocatalysts play crucial roles in their physicochemical properties for efficient light-to-energy conversion. Herein, a novel perovskite $SrTiO_3$ mesocrystal superstructure with well-defined orientation of assembled cubic nanocrystals was synthesized by topotactic epitaxy from TiO_2 mesocrystals through a facile hydrothermal treatment. The $SrTiO_3$ mesocrystal exhibited three times the efficiency for the hydrogen evolution of conventional disordered systems in alkaline aqueous solution. It also exhibited a high quantum yield of 6.7% at 360 nm in overall water splitting and even good durability up to 1 day. Temporal and spatial spectroscopic observations revealed that the synergy of the efficient electron flow along the internal nanocube network and efficient collection at the larger external cubes produces remarkably long-lived charges for enhanced photocatalysis.

Transition-metal-based oxides sharing the perovskite structure are of scientific and technological interest for innovative applications owing to their remarkable physicochemical properties.[1] As a prototypical perovskite, strontium titanate ($SrTiO_3$) with a cubic crystal structure has attracted growing attention in the fields of electromagnetic devices[2] and solar energy conversion systems.[3] With the prospect of further reducing human energy usage and alleviating environmental pollution,[4] heterogeneous solid photocatalysts have been expected to exhibit promising solar-to-chemical energy conversion from water since 1972.[5] To promote the reaction efficiency, numerous strategies have been developed including band engineering,[6] morphology tailoring,[7] co-catalysts assistance,[8] and reaction environment optimization.[9] For instance, La- and Rh-codoped $SrTiO_3$ has been shown to work as an efficient hydrogen evolution reaction (HER) photocatalyst for overall water splitting under visible-light irradiation.[10] Wang et al. incorporated this material into photocatalyst sheet systems with an oxygen evolution photocatalyst (Mo-doped $BiVO_4$) and a Au layer in which good electric contacts between the particulate semiconductors and Au are necessary to reduce the resistance and thus increase reaction efficiency.[11] For the development of more active $SrTiO_3$-based photocatalysts, it is crucial to seek a versatile route for the structure and property design. Novel hybrids of $SrTiO_3$ with TiO_2 have been developed that exhibit improved photoelectrochemical and photocatalytic performances,[12] and it may be anticipated that the efficiency and selectivity of their photocatalytic reactions are governed by the physicochemical characteristics of $SrTiO_3$ with tailored crystal facets and morphologies.[13] However, there remain challenges that are relevant to the fabrication of the organized assembly of such structure-controlled nanoparticles up to the micrometer scale.

With the development of mesocrystal family,[14] TiO_2 mesocrystals (TMCs), which consist of nanocrystal building blocks, have exhibited remarkably improved performance compared to that of the disordered system owing to their efficient charge transfer and separation along the adjacent nanoparticles.[15] Very recently, the epitaxial integration of $SrTiO_3$ from TiO_2 has attracted interest due to the scientific and technological importance of oxide interface engineering.[13b,16] However, exploiting topotactic synthesis techniques to design and fabricate Ti-based ternary perovskite oxides with mesocrystal superstructures, and thus performing detailed investigations into the superstructure-dependent activity in solar energy conversion, is still a challenge.

Herein, we for the first time synthesized $SrTiO_3$ mesocrystals (SMCs) by topotactic epitaxy from TMCs. Topotactic epitaxy, which is a new synthesis method, is a chemical solid-state reaction such that the orientations of the epitaxially grown product crystals are determined by the orientation of the initial crystals. The SMCs, which exhibited synergetic integration of an internal nanocube network and larger external nanocubes, showed superior activity in the HER and overall water splitting than disordered samples. Time-resolved diffuse reflectance (TDR) spectroscopy and single-particle photoluminescence (PL) imaging revealed that the higher activity of the SMCs was due to efficient interparticle charge transfer along the ordered internal nanocubes terminated at the larger active external cubes, allowing the superior water splitting.

SMCs were synthesized by topotactic epitaxy from TMCs via a simple hydrothermal treatment (Figure 1a). Starting from sheet-like TMCs (0 h), which consist of assembled anatase TiO_2 nanocrystals with dominant {001} facets, Sr^{2+} ions from $Sr(OH)_2$ react with TiO_2 in alkaline solution to form an epitaxial overlayer of $SrTiO_3$ grains at the interface (Figure S1) via the dissolution-precipitation processes (6 h).[13b] When one nanocrystal in the SMC-6 sample (Figure S1b) was inspected with high-resolution TEM (HRTEM), it was seen that the TiO_2 is heterogeneously depleted by $SrTiO_3$ in accordance with the corresponding diffraction patterns obtained by fast Fourier transform (FFT) of the HRTEM images at different locations. During nucleation and crystal growth (12-24 h), the cubic $SrTiO_3$ nanocrystals with ordered orientation are constructed, followed by an increase in

[a] Dr. P. Zhang, Prof. M. Fujitsuka, Prof. T. Majima
The Institute of Scientific and Industrial Research (SANKEN), Osaka University
Mihogaoka 8-1, Ibaraki, Osaka 567-0047, Japan
E-mail: majima@sanken.osaka-u.ac.jp
[b] Mr. T. Ochi, Prof. Y. Kobori, Prof. T. Tachikawa,
Department of Chemistry, Graduate School of Science, Kobe University
1−1 Rokkodai-cho, Nada-ku, Kobe 657−8501, Japan
E-mail: tachikawa@port.kobe-u.ac.jp
[c] Prof. Y. Kobori, Prof. T. Tachikawa,
Molecular Photoscience Research Center, Kobe University
1−1 Rokkodai-cho, Nada-ku, Kobe 657−8501, Japan
E-mail: tachikawa@port.kobe-u.ac.jp
[d] Prof. Takashi Tachikawa
PRESTO, Science and Technology Agency (JST),
24-1-8 Honcho Kawaguchi, Saitama 332-0012, Japan

Supporting information for this article is given via a link at the end of the document.

WILEY-VCH

crystallinity. Upon prolonging the hydrothermal time to 36 h, the $SrTiO_3$ grains at the external surfaces of the mesocrystals, i.e., the outer $SrTiO_3$ nanocrystals, gradually grow into larger cubic crystals, resulting in a gradual increase in thickness from 185 nm for the initial TiO_2 to 300 nm (Figure S2). With an increase in aging time from 48 to 60 h, SMCs decorated with much larger nanocubes are finally obtained, with a concomitant thickness increase up to ~360 nm. During the crystallographic epitaxy between the anatase and perovskite structures in alkaline hydrothermal growth, OH^- will neutralize H^+ adsorbed on the O-terminated {001} facets of the TMCs, leading to growth along the [001] axis and exposure of the dominant {100} facets on the SMCs. To model the epitaxial growth, the fundamental unit cell of $SrTiO_3$ (100)-terminated TiO_2 (001) is shown to take into account the interface and surface in epitaxial orientation (Figure 1b). The chemical bonds formed at the interface of $TiO_2/SrTiO_3$ from the structural distortion of TiO_6 octahedra are assumed to be important in determining the final phase of the perovskite structure.[17] Half of the O at the surface of $SrTiO_3$ is bonded to Ti of anatase TiO_2 (site 1), while Ti at the surface of $SrTiO_3$ is also bonded to the O of TiO_2 (site 2).[17a,b] The resulting orientation is the [001] axis of anatase being parallel to the [100] axis of $SrTiO_3$, because of the very small in-plane lattice mismatch between $SrTiO_3$ (cubic crystal, a = 0.39 nm) and TiO_2 (tetragonal crystal, a = b = 0.38 nm, c = 0.95 nm) of around 3%.

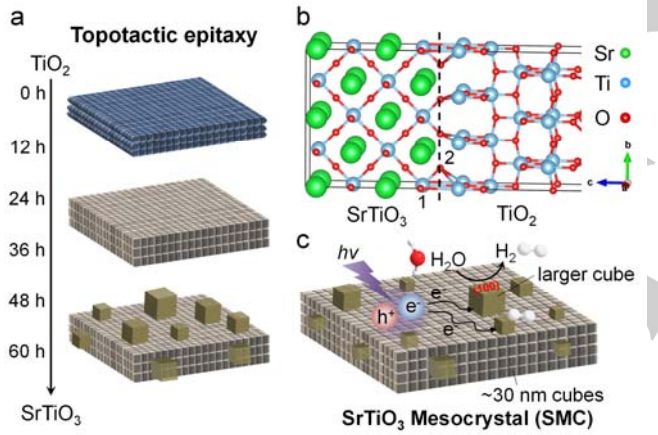

Figure 1. (a) Schematic representation of the topotactic epitaxy of $SrTiO_3$ mesocrystals (SMCs) from TiO_2 mesocrystals (TMCs). (b) Model of the interface structure between an SMC and a TMC. (c) Anisotropic electron transport from the inside to the outside of an SMC, which consists of aligned nanocubes with dominant {100} facets. The symbols e^- and h^+ indicate photogenerated electrons and holes, respectively.

From the structural features of the SMCs, the photocatalytic mechanism and charge transfer processes are proposed as illustrated in Figure 1c. The well-ordered superstructure facilitates spatial charge separation throughout the long-distance electron transport along the ordered adjacent nanocubes inside the mesocrystal, and the charges move to the larger external nanocubes with active {100} facets, where H^+ is reduced to generate H_2 under UV-light irradiation.[18]

To clarify the superstructure of the SMCs, representative FESEM and TEM images of SMCs after 48 h hydrothermal growth were selected, as summarized in Figure 2. The plate-like architectures of the SMCs (3–6 μm in size) with rich mesopores are clearly visible in Figure 2a. The magnified FESEM image (Figure 2b) shows that the SMC superstructures are composed of nanocubes with interconnected porosity. The TEM analysis further reveals that the external surfaces of the SMCs are covered with larger nanocubes (200 nm) rather than the small nanocubes (30 nm) assembled inside the mesocrystal (Figure 2c and S3). As demonstrated in Figure 2c, the selective area electron diffraction (SAED) patterns obtained at different locations, i.e., near the center and edge (see red circles), represent single-crystal-like spots, confirming that the SMCs comprise crystallographically aligned nanocrystals, i.e., the mesocrystal. It should be noted here that the orientation of the crystals is maintained during the epitaxial structural conversion and subsequent crystal growth. Indeed, this is a feature of topotactic epitaxy and is obviously attributed to particle-to-particle interactions in the mesocrystal. The lattice spacing of the nanocubes is approximately 0.276 nm, which corresponds to the (110) plane of $SrTiO_3$ (Figure 2d). The elemental mapping by SEM-EDX confirms that the SMCs have similar spatial distributions of Sr, Ti, and O elements (Figure S4).

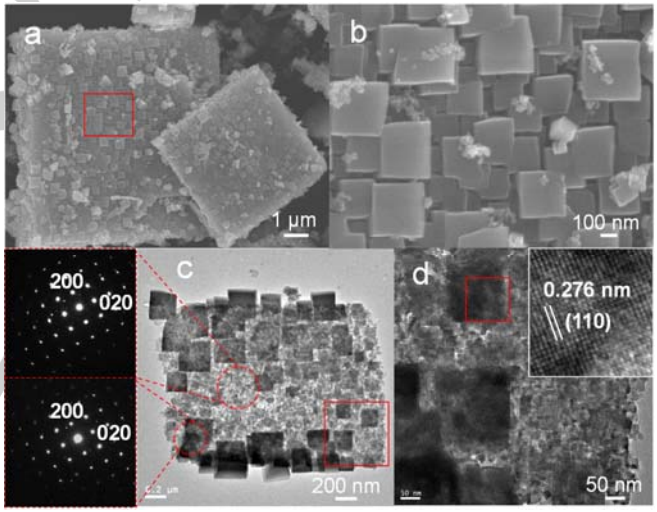

Figure 2. (a) FESEM image of SMC-48 and (b) its high-resolution image. (c) TEM images of SMC-48 with SAED from near the center and at the edge (red circle), and (d) the high-resolution images of the red-squared sections in panels (c) and (d).

The crystal evolution of SMCs during hydrothermal treatment was closely monitored using powder X-ray diffraction (XRD) (Figure S5). It can be seen that all the diffraction peaks of SMC-12 are well indexed to cubic $SrTiO_3$ with negligible impurity anatase phase.[19] As the aging time increases from 24 h to 60 h, the XRD peaks of $SrTiO_3$ become stronger and sharper along with the disappearance of the anatase phase, indicating the total depletion of TiO_2. The corresponding structural conversion from TMCs to SMCs was confirmed by TEM (Figure S6), which is coincident with the illustration in Figure 1a.[20] During the crystal growth, the surface area gradually decreases from 27.8 to 9.7 $m^2\ g^{-1}$ (Table S1 and Figure S7), indicating that the particles shrink and undergo fusion.[21] The structures and properties of

SMCs were further characterized by X-ray photoelectron spectroscopy (XPS), steady-state UV-visible absorption spectroscopy, and electrochemical methods (Figures S8-11).

The superstructure-related photocatalytic activities were first optimized over the series of SMCs with different aging times (Figure S12). In the presence of 5 M NaOH, the performances of all the samples are improved (Figure 3a) without the use of co-catalysts such as Pt nanoparticles. This is because the generated holes quickly transfer to hydroxide ions adsorbed on the surface to generate hydroxyl radicals that oxidize methanol molecules in solution.[9b] Among the samples, the highest photocatalytic activity is achieved on SMC-48 in alkaline solution, which results in an HER rate of 0.50 μmol·h^{-1}, around three times higher than that of Nano (0.17 μmol·h^{-1}). The apparent quantum efficiencies (AQEs) for HER were 2.1 % at 360 nm and 1.2% at 380 nm for SMC-48, and 1.1 % at 360 nm and 0.6% at 380 nm for Nano (Figure S10, right axis), clearly indicating the superior performance of SMCs than the conventional nanoparticle system. When SMC-48 is crushed by grinding prior to testing, the activity decreases to 20% of that for pristine SMC-48, indicating the important role of the superstructure (Figure 3b and S13). The pH dependence of the photocurrent generation follows the same trend as that for the HER (Figure 3c), again demonstrating the highest activity of SMC-48 and the alkalinity-dependency of the photocatalytic efficiency.

To further demonstrate the potential of the superstructure-based system, overall water splitting was investigated for the photocatalysts with co-catalyst modification.[10] The deposition of mixed-oxide $Rh_{2-x}Cr_xO_3$ was confirmed by XPS (Figure S14). It was noted that the SMC-48 with optimized $Rh_{2-x}Cr_xO_3$ (Rh 1 wt%, Cr 1 wt%) exhibits a superior activity than Nano after 5 h (Figure 3d and S15). It maintained the good durability up to 1 day after 5 cycle tests (25 h) without activity decrease (Figure 3e). The AQE of SMC-48 obtained at 360 nm was 6.7%, while that of Nano was almost zero. This positive incorporation will stimulate one to employ the superstructure to improve the efficiency of various photocatalytic reactions.

To understand the photo-charge dynamics, femtosecond TDR measurements were carried out. Upon 330-nm laser excitation of SMC-48 and Nano, as shown in Figure S16, a broad absorption band appears in the near-infrared region, which is superimposed with trapped holes and electrons in $SrTiO_3$.[22] The transient absorption of Nano decays rapidly when compared with that of SMC-48. The time profiles of absorption probed at 900 nm were fitted using multiexponential functions to evaluate the decay kinetics (Figure S16c and Table S2). The data for SMC-48 was fitted with two components (τ_2 and τ_3) without a few picoseconds component (τ_1). Surprisingly, 30% of the electrons generated in SMC-48 still survive at 2.5 ns after the flash (Table S2). This yield is 1.4 times higher than that of Nano. The trapped charge carriers migrate via trapping-detrapping processes along the nanoparticle network, resulting in prolonged charge lifetime and thus efficient photocatalysis. The SMC exhibits this benefit rather than Nano, which undergoes prompt intraparticle charge recombination within ~100 ps.[23]

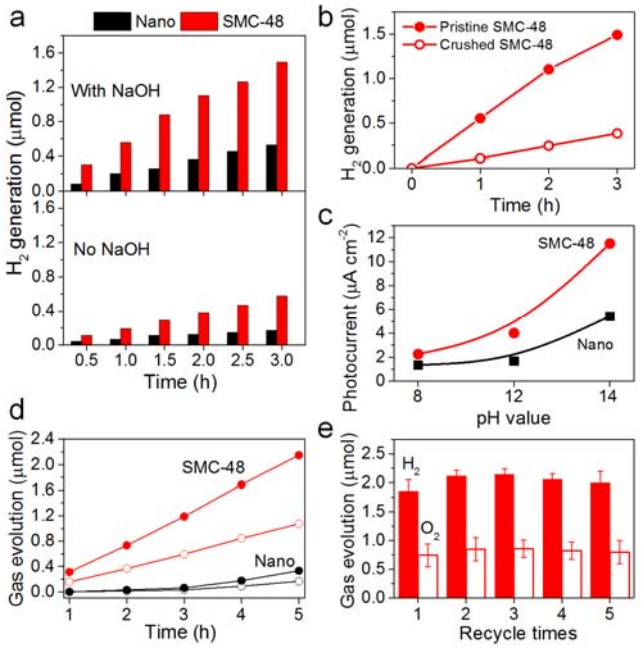

Figure 3. (a) Hydrogen generation over the photocatalysts (1 mg) in 2 mL 20% methanol-water mixtures with and without the addition of 5 M NaOH under UV-light irradiation. (b) Hydrogen generation from the photocatalysts before and after grinding. (c) Photocurrent generated by the photocatalysts as a function of the pH value. (d) Gas evolution during the water splitting reaction of H_2 (solid circles) and O_2 (open circles). (e) The durability of SMC-48 in water splitting after each 5 h.

The relationship between the mesocrystal superstructure and charge carrier dynamics remains unresolved. Interestingly, SMC-24 shows much lower activity than SMC-48 in spite of its higher surface area and well-ordered structure (Table S1 and Figure S6). We applied single-particle spectroelectrochemistry (Figure 4a)[24] to determine the active sites on the mesocrystal surface and reveal the role of structural disorders.

Figures 4b and 4c show typical PL images of SMCs under 405-nm laser irradiation. According to the literature,[13e,25] the observed broad PL band in the visible region is attributable to various defects in $SrTiO_3$ (Figure 4d). Thus, the emitting sites allow us to assess the spatial distribution of effective trapping/reactive sites of the charges. Interestingly, SMC-24 exhibits weak and uniform PL over the entire crystal except edges with structural imperfections or disorders, while SMC-48 presents a limited number of emitting sites on its surface decorated with several-hundred-nanometers particles (Figure S6). Furthermore, as shown in Figure 4e, a significant increase in the PL intensity is observed at the larger nanocube without significant spectral shape change under applied negative potentials of −0.80 V vs Ag/AgCl (= −0.25 V vs RHE), which is more positive than the conduction band (CB) edge of $SrTiO_3$ and corresponds to the trap states originating from oxygen vacancies.[26] The negative bias-induced PL is thus indicative of the radiative recombination of trapped electrons at the oxygen vacancies and mobile holes (i.e., $V_O^+ + h^+ \rightarrow$ PL, where V_O^+ and h^+ indicate oxygen vacancy with one electron and hole, respectively). These results strongly support our model in which the photogenerated electrons migrate via the nanocube

networks inside the mesocrystals and are captured at the larger nanocubes on the external surface. A decrease in the PL intensity with negative potentials over −1 V vs Ag/AgCl might be due to nonradiative recombination between excess electrons in the CB and holes due to the nature of the indirect band gap.[24b,27]

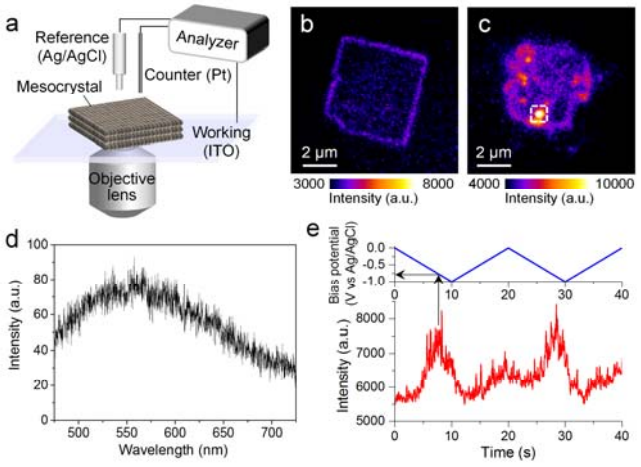

Figure 4. (a) Illustration of the experimental setup for single-particle spectroelectrochemistry. PL images of (b) SMC-24 and (c) SMC-48 on an ITO-coated cover glass in Ar-saturated aqueous solution of Na_2SO_4 (0.2 M, pH 6.0) under 405 nm laser irradiation without an applied potential. (d) Typical PL spectrum of SMC-48. (e) Applied potential dependence of the PL intensity obtained for SMC-48. The region tested is shown by a box in panel c.

It is generally believed that a well-defined superstructure can deliver photo-charges more efficiently than disordered systems such as nanoparticle aggregates, and is thus attractive for improving the efficiency of solar energy conversion.[15] However, photo-charges must be separately collected at specific active sites for further reactions prior to charge recombination. One of the main themes of the present study is that controlled structural disorder is necessary to spatially separate sites for charge transport and catalysis for efficient photocatalytic reactions, as illustrated in Figure 1c. Once the charges are captured on the larger external nanocubes, they would hardly return to the internal 30-nm nanocubes due to the limited contact interfaces and/or Schottky depletion space-charge layers (approximately several tens of nanometers to a hundred nanometers in width) at grain boundaries.[28] The higher electron density is kinetically favorable for two-step successive reduction of protons to generate H_2, although it is still challenging to determine the intrinsic redox sites on or inside the three-dimensional architecture at the single-particle level. Furthermore, the exposure of the active nanocubes enhances accessibility of target ions/molecules[29] and suppresses an undesired accumulation of the product gas inside the mesopores, decreasing the effective area,[30] during photocatalysis.

In conclusion, novel $SrTiO_3$ mesocrystal superstructures were successfully synthesized by topotactic epitaxy from precursor TiO_2 mesocrystals via a simple hydrothermal treatment. By means of TDR measurements and single-particle PL imaging, it was demonstrated that the well-ordered assembly of $SrTiO_3$ nanocubes plays a key role in prolonged charge lifetimes owing to efficient interparticle electron transfer, thus remarkably enhancing photocatalytic performance. The design principle of perovskite-type mesocrystals and the mechanistic insight into the heterogeneous charge transfer reactions occurring in the superstructure system will provide new strategies for the fields of photocatalysis and optoelectronics. In particular, it would be of great interest to develop doped perovskite oxide mesocrystals with visible-light responsivity for achieving efficient solar energy conversion.

Acknowledgements

This work has been partly supported by Grants-in-Aid for Scientific Research (25220806, 25288035, 15H03771, and others) from the Ministry of Education, Culture, Sports, Science and Technology (MEXT) of the Japanese Government. This work was performed under the Cooperative Research Program of "Network Joint Research Center for Materials and Devices".

Keywords: Interfacial charge transfer • Mesocrystal • Photocatalysis • Superstructure • Water splitting

[1] a) C. H. Ahn, J. M. Triscone, J. Mannhart, *Nature* **2003**, *424*, 1015-1018; b) J. Mannhart, D. G. Schlom, *Science* **2010**, *327*, 1607-1611.

[2] M. Huijben, A. Brinkman, G. Koster, G. Rijnders, H. Hilgenkamp, D. H. A. Blank, *Adv. Mater.* **2009**, *21*, 1665-1677.

[3] a) F. T. Wagner, G. A. Somorjai, *Nature* **1980**, *285*, 559-560; b) R. Konta, T. Ishii, H. Kato, A. Kudo, *J. Phys. Chem. B* **2004**, *108*, 8992-8995; c) S. Y. Yang, J. Seidel, S. J. Byrnes, P. Shafer, C. H. Yang, M. D. Rossell, P. Yu, Y. H. Chu, J. F. Scott, J. W. Ager, III, L. W. Martin, R. Ramesh, *Nat. Nanotechnol.* **2010**, *5*, 143-147; d) J. M. P. Martirez, S. Kim, E. H. Morales, B. T. Diroll, M. Cargnello, T. R. Gordon, C. B. Murray, D. A. Bonnell, A. M. Rappe, *J. Am. Chem. Soc.* **2015**, *137*, 2939-2947.

[4] a) X. Chen, S. Shen, L. Guo, S. S. Mao, *Chem Rev* **2010**, *110*, 6503-6570; b) A. Kudo, Y. Miseki, *Chem. Soc. Rev.* **2009**, *38*, 253-278.

[5] A. Fujishima, K. Honda, *Nature* **1972**, *238*, 37-38.

[6] a) Z. Zhang, J. T. Yates, Jr., *Chem. Rev.* **2012**, *112*, 5520-5551; b) R. Asahi, T. Morikawa, H. Irie, T. Ohwaki, *Chem. Rev.* **2014**, *114*, 9824-9852.

[7] a) C. Burda, X. Chen, R. Narayanan, M. A. El-Sayed, *Chem. Rev.* **2005**, *105*, 1025-1102; b) G. Liu, H. G. Yang, J. Pan, Y. Q. Yang, G. Q. Lu, H.-M. Cheng, *Chem. Rev.* **2014**, *114*, 9559-9612.

[8] a) J. Ran, J. Zhang, J. Yu, M. Jaroniec, S. Z. Qiao, *Chem. Soc. Rev.* **2014**, *43*, 7787-7812; b) J. Yang, D. Wang, H. Han, C. Li, *Acc. Chem. Res.* **2013**, *46*, 1900-1909.

[9] a) J. Schneider, M. Matsuoka, M. Takeuchi, J. Zhang, Y. Horiuchi, M. Anpo, D. W. Bahnemann, *Chem. Rev.* **2014**, *114*, 9919-9986; b) S. Ouyang, H. Tong, N. Umezawa, J. Cao, P. Li, Y. Bi, Y. Zhang, J. Ye, *J. Am. Chem. Soc.* **2012**, *134*, 1974-1977.

[10] a) Q. Wang, T. Hisatomi, S. S. K. Ma, Y. Li, K. Domen, *Chem. Mater.* **2014**, *26*, 4144-4150; b) K. Maeda, K. Teramura, D. Lu , T. Takata, N. Saito, Y. Inoue, K. Domen, *J. Phys. Chem. B*, **2006**, *110*, 13753-13758; c) K. Maeda, K. Teramura, D. Lu, T. Takata, N. Saito, Y. Inoue, K. Domen, *Nature*, **2006**, *440*, 295; d) Y. Ham, T. Hisatomi, Y. Goto, Y. Moriya, Y. Sakata, A. Yamakata, J. Kubota, K. Domen, *J. Mater. Chem. A*, **2016**, *4*, 3027-3033.

[11] Q. Wang, T. Hisatomi, Q. Jia, H. Tokudome, M. Zhong, C. Wang, Z. Pan, T. Takata, M. Nakabayashi, N. Shibata, Y. Li, I. D. Sharp, A. Kudo, T. Yamada, K. Domen, *Nat Mater* **2016**, *15*, 611-615.

[12] a) K. A. Mueller, H. Burkard, *Phys. Rev. B: Condens. Matter* **1979**, *19*, 3593-3602; b) Y. Xin, J. Jiang, K. Huo, T. Hu, P. K. Chu, *ACS Nano* **2009**, *3*, 3228-3234; c) S. Burnside, J.-E. Moser, K. Brooks, M. Graetzel, D. Cahen, *J. Phys. Chem. B* **1999**, *103*, 9328-9332; d) I. Hod, M. Shalom, Z. Tachan, S. Ruhle, A. Zaban, *J. Phys. Chem. C* **2010**, *114*, 10015-10018; e) X. Zhang, K. Huo, L. Hu, Z. Wu, P. K. Chu, *J. Am. Ceram. Soc.* **2010**, *93*, 2771-2778; f) J.

Zhang, J. H. Bang, C. Tang, P. V. Kamat, *ACS Nano* **2010**, *4*, 387-395.

[13] a) X. Wei, G. Xu, Z. Ren, C. Xu, W. Weng, G. Shen, G. Han, *J. Am. Ceram. Soc.* **2010**, *93*, 1297-1305; b) V. Kalyani, B. S. Vasile, A. Ianculescu, M. T. Buscaglia, V. Buscaglia, P. Nanni, *Cryst. Growth Des.* **2012**, *12*, 4450-4456; c) N.-H. Park, Y. Wang, W.-S. Seo, F. Dang, C. Wan, K. Koumoto, *CrystEngComm* **2013**, *15*, 679-685; d) G. Xu, X. Huang, Y. Zhang, S. Deng, X. Wei, G. Shen, G. Han, *CrystEngComm* **2013**, *15*, 7206-7211; e) A. E. Souza, G. T. A. Santos, B. C. Barra, W. D. Macedo, Jr., S. R. Teixeira, C. M. Santos, A. M. O. R. Senos, L. Amaral, E. Longo, *Cryst. Growth Des.* **2012**, *12*, 5671-5679.

[14] a) T. Tachikawa, T. Majima, *NPG Asia Mater.* **2014**, *6*, e100; b) L. Bergstroem, E. V. Sturm, G. Salazar-Alvarez, H. Cölfen, *Acc. Chem. Res.* **2015**, *48*, 1391-1402; c) E. V. Rosseeva, H. Cölfen, *Chem. Soc. Rev.* **2016**, *45*, 5821-5833.

[15] a) Z. Bian, T. Tachikawa, T. Majima, *J. Phys. Chem. Lett.* **2012**, *3*, 1422-1427; b) Z. Bian, T. Tachikawa, W. Kim, W. Choi, T. Majima, *J. Phys. Chem. C* **2012**, *116*, 25444-25453; c) Z. Bian, T. Tachikawa, P. Zhang, M. Fujitsuka, T. Majima, *J. Am. Chem. Soc.* **2014**, *136*, 458-465.

[16] a) T. Yu, W.-l. Hu, L. Jia, X. Tan, J. Huang, X. Huang, *Ind. Eng. Chem. Res.* **2015**, *54*, 8193-8200; b) E. Guo, L. Yin, *J. Mater. Chem. A* **2015**, *3*, 13390-13401; c) T. Cao, Y. Li, C. Wang, C. Shao, Y. Liu, *Langmuir* **2011**, *27*, 2946-2952.

[17] a) apos, N. R. Amico, G. Cantele, D. Ninno, *Appl. Phys. Lett.* **2012**, *101*, 141606; b) S. A. Chambers, T. Ohsawa, C. M. Wang, I. Lyubinetsky, J. E. Jaffe, *Surf. Sci.* **2009**, *603*, 771-780; c) A. Lotnyk, S. Senz, D. Hesse, *Thin Solid Films* **2007**, *515*, 3439-3447.

[18] a) J. L. Giocondi, G. S. Rohrer, *J. Am. Ceram. Soc.* **2003**, *86*, 1182-1189; b) J. L. Giocondi, P. A. Salvador, G. S. Rohrer, *Top. Catal.* **2007**, *44*, 529-533.

[19] a) C. W. Kim, S. P. Suh, M. J. Choi, Y. S. Kang, Y. S. Kang, *J. Mater. Chem. A* **2013**, *1*, 11820-11827; b) J. Ng, S. Xu, X. Zhang, H. Y. Yang, D. D. Sun, *Adv. Funct. Mater.* **2010**, *20*, 4287-4294.

[20] T. Shibata, H. Takano, Y. Ebina, D. S. Kim, T. C. Ozawa, K. Akatsuka, T. Ohnishi, K. Takada, T. Kogure, T. Sasaki, *J. Mater. Chem. C* **2014**, *2*, 441-449.

[21] a) P. Zhang, T. Tachikawa, M. Fujitsuka, T. Majima, *Chem. Commun.* **2015**, *51*, 7187-7190; b) P. Zhang, M. Fujitsuka, T. Majima, *J. Energy. Chem.* **2016**, *25*, 917-926.

[22] a) A. Yamakata, J. J. M. Vequizo, M. Kawaguchi, *J. Phys. Chem. C* **2015**, *119*, 1880-1885; b) A. Yamakata, H. Yeilin, M. Kawaguchi, T. Hisatomi, J. Kubota, Y. Sakata, K. Domen, *J. Photochem. Photobiol. A* **2015**, *313*, 168-175.

[23] P. Zhang, T. Tachikawa, M. Fujitsuka, T. Majima, *Chem. Commun.* **2015**, *51*, 7187-7190.

[24] a) T. Tachikawa, T. Majima, *J. Am. Chem. Soc.* **2009**, *131*, 8485-8495; b) T. Tachikawa, T. Ochi, Y. Kobori, *ACS Catal.* **2016**, *6*, 2250-2256.

[25] a) A. Janotti, J. B. Varley, M. Choi, C. G. Van de Walle, *Phys. Rev. B Condens. Matter Mater. Phys.* **2014**, *90*, 085202/085201-085202/085206, 085206 pp; b) D. Kan, T. Terashima, R. Kanda, A. Masuno, K. Tanaka, S. Chu, H. Kan, A. Ishizumi, Y. Kanemitsu, Y. Shimakawa, M. Takano, *Nat. Mater.* **2005**, *4*, 816-819.

[26] a) M. Choi, F. Oba, Y. Kumagai, I. Tanaka, *Adv. Mater.* **2013**, *25*, 86-90; b) J. M. Bolts, M. S. Wrighton, *J. Phys. Chem.* **1976**, *80*, 2641-2645.

[27] K. van Benthem, C. Elsasser, R. H. French, *J. Appl. Phys.* **2001**, *90*, 6156-6164.

[28] a) R. Waser, R. Hagenbeck, *Acta Mater.* **2000**, *48*, 797-825; b) M. M. Waegele, X. Chen, D. M. Herlihy, T. Cuk, *J. Am. Chem. Soc.* **2014**, *136*, 10632-10639.

[29] L. Soleymani, Z. Fang, E. H. Sargent, S. O. Kelley, *Nat. Nanotechnol.* **2009**, *4*, 844-848.

[30] S. Hernandez, G. Barbero, G. Saracco, A. L. Alexe-Ionescu, *J. Phys. Chem. C* **2015**, *119*, 9916-9925.

WILEY-VCH